A Miniature Water Jumping Robot Based on Accurate Interaction Force Analysis

Jihong Yan, *Member, IEEE*, Xin Zhang, *Student Member, IEEE*, Kai Yang, and Jie Zhao, *Member, IEEE*

***Abstract*—Water jumping motion extends the robot's movement space and flexibility. However, the jumping performance is influenced by multiple factors such as driving force, rowing trajectory, and robot structure. The interaction force between the robot and water surface is complicated due to water deformation, and the difficulty of the water jumping increases with the robot's scale. This article designs a miniature water jumping robot with rowing driving legs. The hydrodynamic model between driving legs and water is established based on the modified Wagner theory with consideration of water surface deformation. Particularly, the dynamic model of the robot for the whole jumping process is also developed related to multiple factors. Then, the jumping performance is improved by optimizing the energy storage modality, rowing trajectory, and supporting leg shapes through the theoretical analysis and experiments. The fabricated robot weights 91 g, and its length, width, and height are 220, 410, and 95 mm, respectively. The maximum water jumping height and distance are 241 and 965 mm.**

***Index Terms*—Hydrodynamic, robot–water surface interaction, trajectory optimization, water jumping robot.**

I. Introduction

MINIATURE jumping robots have become a research hotspot in the robotics field due to their superior concealability, mobility, and environmental adaptability, and they are mainly divided into land jumping robots and water jumping robots according to the jumping media. Land has sufficient stiffness to provide adequate support force and friction for the robot [1], [2], [3], [4]. However, water surface is a flexible supporting system, and water jumping is a sophisticated robot–fluid interaction process. The splash generated by the rapid rowing of the driving legs cause energy dissipation. The water surface deformation will affect the force and pitch attitude of the robot, and the drag resistance of the supporting system will reduce the jumping performance. It can be seen that there are more factors affecting the water jumping performance and the influence principle is more complicated.

Manuscript received 30 June 2023; revised 26 September 2023; accepted 6 November 2023. Date of publication 13 November 2023; date of current version 29 December 2023. This paper was recommended for publication by Associate Editor C. Sung and Editor M. Yim upon evaluation of the reviewers' comments. This work was supported by the Equipment Pre-Research Application Innovation Project under Grant 62602010202. *(Corresponding author: Jihong Yan.)*

Jihong Yan and Kai Yang are with the State Key Laboratory of Robotics and Systems, Laboratory for Space Environment and Physical Sciences, Harbin Institute of Technology, Harbin 150001, China (e-mail: jhyan@hit.edu.cn; 14b908026@hit.edu.cn).

Xin Zhang and Jie Zhao are with the State Key Laboratory of Robotics and Systems, Harbin Institute of Technology, Harbin 150001, China (e-mail: 2359747812@qq.com; jzhao@hit.edu.cn).

Digital Object Identifier 10.1109/TRO.2023.3332161

The water jumping robots can be divided into surface tension driven robots and water pressure driven robots according to the proportion of dynamic pressure force and surface tension force. Surface tension driven robots [5], [6] are lightweight and are not capable of functional applications in the short term due to their small scale, poor load capacity, and miniaturized integrated manufacturing technology limitations. Water pressure driven robots [7], [8] have larger scale and load capacity to carry miniature sensors, making it more accessible for practical application. Meanwhile the robot's water jumping performance is also restricted by its scale, l_r denotes the robot characteristic size, the dynamic pressure $\propto l_r^2$, while the robot mass $\propto l_r^3$. As the robot scale increases, its weight increases at a higher rate than the driving force. How to optimize the water jumping performance and load capacity within the restricted robot scale and weight is a crucial problem that needs to be solved urgently.

Scholars have conducted numerous studies on the water jumping robots. Zhao et al. [5] developed the world's first water-continuous jumping robot, and they analyzed the effects of energy storage element stiffness and jumping angle on the jumping performance. Koh et al. [6] analyzed the effects of driving torque and speed on the jumping performance. Jiang et al. [7] minimized the torque required for energy storage by optimizing the jumping mechanism size. Traditional water pressure calculation model [9] mainly focused on the influence of hydrostatic pressure and dynamic pressure. The water hexapod walking robots [10], [11], [12] and bionic lizard robots [13], [14], [15], [16], [17] decomposed the driving force into hydrostatic pressure and inertial resistance, which improved the solution accuracy of the driving force.

Despite noteworthy research progress of water jumping robots is achieved, two issues remain underexplored. The first is to develop a dynamic model of the robot's water jumping motion and to analyze the influence of structural parameters on the jumping performance. The energy storage mechanism, rowing trajectory, and water surface deformation are all factors that affect the driving force, and they need to be considered in the hydrodynamic model. The second problem is to optimize the energy storage mechanism and rowing trajectory. The mechanism size and the type of elastic element determine the energy storage capacity and output force. The rowing trajectory mainly affects the component of driving force in each direction. This article aims to address these issues by presenting the design, modeling, and experimentation of a miniature water jumping robot.

The rest of this article is organized as follows. Section II introduces the system components of the robot, and analyzes

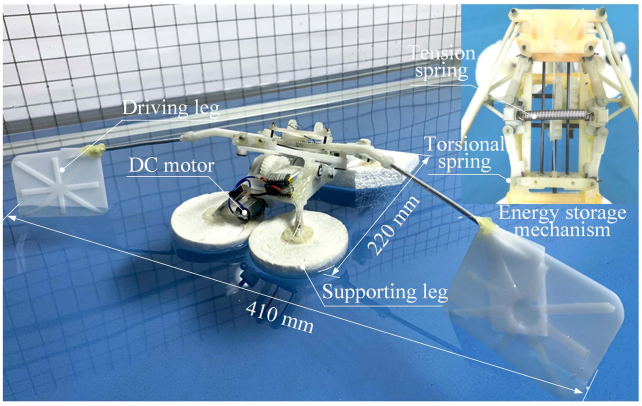

Fig. 1. Prototype of the miniature water jumping robot.

the effect of energy storage mechanism on the energy storage size and output force. Section III establishes the driving force model based on Wagner theory and analyzes the supporting and resistance forces according to the robot's motion posture. In Section IV, the robot's dynamics model for the whole water jumping process is established and the jumping performance is improved by optimizing the rowing trajectory parameters. In Section V, the supporting legs shape is optimized and the water jumping experiments are carried out. Section VI concludes this article.

II. Design and Manufacture

The miniature robot is mainly composed of energy storage, driving and supporting mechanisms, and they need to be elaborately designed to achieve better water jumping performance. The driving force and energy storage capacity are improved by optimizing the mechanism size and energy storage element. The rowing trajectory of the driving legs and the layout of the supporting legs are optimized to improve the water jumping performance. The detailed parameter optimization will be discussed in Section IV. The driving mechanism is designed based on the efficient driving principle and the prototype of the robot is shown in Fig. 1. Its length, width, and height are 220, 410, and 95 mm, respectively, and the weight is 91 g. The body of the robot is made of polyoxymethylene (POM) material and the supporting legs are made of lightweight foam.

A. Energy Storage Mechanism

The six rods are joined at the beginning and end to form a symmetrical hexagon, so that the mechanism will not deflect during the energy storage process. It can convert the linear force of the spring into nonlinear force by combining with the energy storage element. Therefore, hexagonal rod mechanism is widely used in the energy storage mechanism of jumping robots [2], [8], [18], [19]. According to the different types of energy storage elements, it can be categorized into: i) tension spring (Ten), ii) torsion spring (Tor), iii) compression spring (Pre), and iv) tension-torsion spring (Ten-Tor), as shown in Fig. 2(a). It is assumed that the total length of the hexagonal rod mechanism is 152 mm, the minimum rod length is 20 mm,

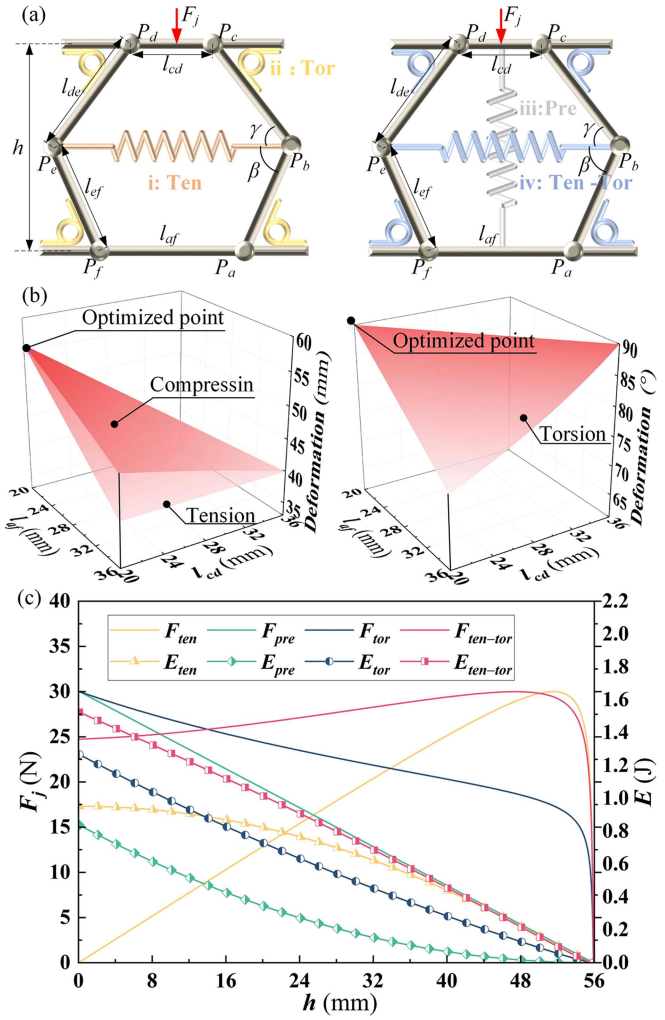

Fig. 2. Schematic of the energy storage mechanism with different energy storage elements. (a) i. tension spring, ii. torsional spring, iii. pressure spring, iv. tension and torsional spring. (b) Deformation of the energy storage mechanism with different rod lengths. (c) F_j and E of the energy storage mechanism with different spring types.

$\angle P_cP_bP_e = \gamma$, $\angle P_aP_bP_e = \beta$, $l_{af} \geq l_{cd}$, and the energy storage mechanism can be compressed to the lowest position (i.e., $l_{af} + 2l_{ab} = l_{cd} + 2l_{bc}$). The output force $\boldsymbol{F_j}$, energy storage capacity E, and the maximum deformation $\mathrm{Def}_{\max}$ can be solved by the hydrostatic equilibrium conditions. As shown in Table I, where k_1, k_2 denote the stiffness of the tension and compression springs respectively, and x_1, x_2 denote their initial lengths. k_3, k_4 denote the stiffness of the upper and lower torsion springs in Fig. 2(a), and ψ_3, ψ_4 denote their initial angles. h denotes the distance between rod P_aP_f and P_cP_d. The effect of the rod length on the maximum deformation is shown in Fig. 2(b), and the deformation is maximum when $l_{af} = l_{cd} = 20$ mm, $l_{ab} = l_{bc} = 28$ mm.

To reduce the weight of the robot, the GA12-N30 dc gear motor with high power to mass ratio was adopted (motor weight 11.8 g, rated torque 0.0156 N·m, power 0.7 W). The reduction ratio of the driving mechanism is 18.67, and the maximum output force is 36.4 N, which will limit stiffness of the energy

TABLE I
OUTPUT FORCE AND ENERGY STORAGE WITH DIFFERENT SPRING TYPES

Spring	F_j	E	Def_{max}
Tension	$\frac{2k_1(l_{cd}+2l_{bc}\cos\gamma-x_1)\sin\gamma\sin\beta}{\sin(\gamma+\beta)}$	$\frac{k_1(l_{cd}+2l_{bc}\cos\gamma-x_1)^2}{2}$	$76\text{-}l_{af}$
Compression	$k_2(x_2-l_{bc}\sin\gamma-l_{ab}\sin\beta)$	$\frac{k_2(x_2-l_{bc}\sin\gamma-l_{ab}\sin\beta)^2}{2}$	$\frac{76-l_{af}+\sqrt{(76-l_{cd})^2+(l_{af}-l_{cd})^2}}{2}$
Torsion	$\frac{2(k_3(\psi_3-\gamma)l_{ab}\sin\beta+k_4(\psi_4-\beta)l_{bc}\sin\gamma)}{l_{ab}l_{bc}\sin(\gamma+\beta)}$	$k_3(\psi_3-\gamma)^2+k_4(\psi_4-\beta)^2$	$\arccos\frac{l_{af}-l_{cd}}{76-l_{cd}}$

TABLE II
PARAMETERS OF THE ENERGY STORAGE MECHANISM WITH DIFFERENT SPRING TYPES

Spring	Original size		Stiffness		Energy storage (J)		
	Ten, Pre (mm)	Tor (rad)	Ten, Pre (N·m)	Tor (N·m/rad)	E	E_{ten}, E_{pre}	E_{tor}
Tension	23.345	---	686.8	---	0.952	0.952	---
Compression	55.9	---	537.6	---	0.837	0.837	---
Torsion	---	1.511	---	0.278	1.267	---	1.267
Ten-Tor	23.345	1.511	346	0.229	1.524	0.48	1.044

storage element. In this article, we assume that the maximum output force during the energy release process is 30 N, the actual compression range of the energy storage mechanism $h \in [0.1, 55.9]$ mm, and the energy can be completely released (i.e., $\boldsymbol{F}_j = 0$ when $h = 55.9$ mm), the original length, elasticity coefficient, and the energy storage capacity of the hexagonal rod mechanism are solved as shown in Table II.

The energy storage mechanism is the core of the robot, it has a crucial impact on the jumping performance in terms of energy storage size and output force. Fig. 2(c) shows the relationship between $\boldsymbol{F}_j$, E, and h. Pre and Tor have the largest output force at the initial stage of energy release, and then the driving force gradually decreases, while the driving force of Ten gradually increases during the energy release process. Therefore, the combination of Ten with Pre or Tor can improve the driving force. Ten–Tor integrates the characteristics of both elements, and its energy storage size is 1.6 times that of Ten and 1.2 times that of Tor. However, the combination of Ten and Pre was not chosen for two reasons: i) Pre has a smaller output force and energy storage size compared to Tor. ii) Ten and Pre are installed in a crossed position, which may interfere during the energy release process. Thus, the utilization of Ten–Tor energy storage mechanism is more favorable to improve the water jumping performance.

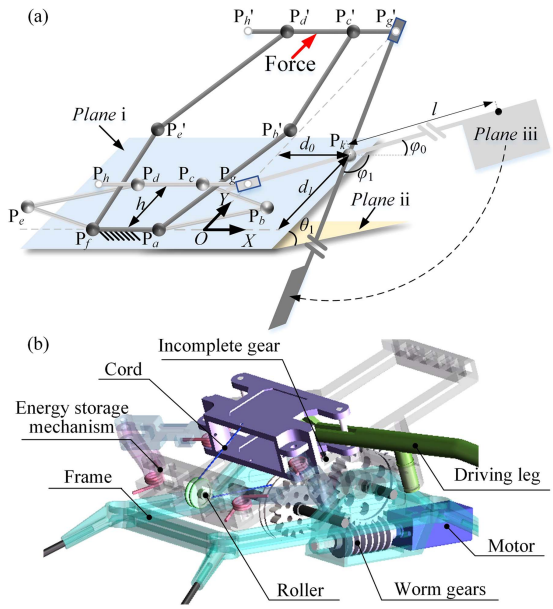

Fig. 3. Driving schematic and mechanism of the miniature water jumping robot. (a) Robot driving schematic. (b) Driving mechanism of the robot, it is mainly composed of motor, worm gears, incomplete gear, energy storage mechanism, cord, frame, and driving leg.

B. Driving and Supporting Mechanism

Fig. 3(a) shows the driving schematic of the jumping mechanism, where *Plane* i is the energy storage mechanism plane, *Plane* ii and iii are the water surface and driving legs plane, respectively, *Plane* iii is perpendicular to *Plane* i, and the angle between *Plane* i and *Plane* ii is θ_1. The symmetrical hexagonal rod mechanism is applied to the energy storage mechanism, the light gray and dark gray contours indicate the start and end states of energy release process. d_0 and d_1 denote the distances from point P_k to $P_gP'_g$ and P_aP_f. l denotes the length of driving legs. We constrain the hexagonal rod mechanism to move only in the *OY* direction, and the P_aP_f rod is fixed to the Plane *i*. The driving leg can swing around the point P_k, and it intersects with the P_cP_d rod at the point P_g, which constitutes the guide rod mechanism. In this way, the hexagonal rod mechanism moves upward and drives the plate swing downward to strike the water.

To maintain the driving efficiency of the guide rod mechanism, the transmission angle of the driving mechanism is not less

than 30°, and the swing angle range is not less than 90° (i.e., $\varphi_0 > 30°, \varphi_1 > 30°, \varphi_0 + \varphi_1 \geq 90°$). Fig. 3(b) shows the driving mechanism of the robot. The motor drives incomplete gear and wire wheel through worm gear, the wire wheel is connected to the energy storage mechanism through cord. When the incomplete gear engages to the toothless field, the energy storage mechanism quickly releases energy and drives the plate to strike water by the guide rod mechanism. The energy storage mechanism is equipped with guide rods to improve the mechanism stiffness, and the rotating joints are geared to improve the synchronization motion.

The miniature water motion robots commonly adopt hollow spheres or ellipsoids as supporting legs to reduce the motion resistance. The fore supporting legs leave water surface first during the jumping process, it requires less drag resistance for fore supporting legs and sufficient support force for rear supporting legs. Therefore, the fore supporting leg is designed as two hemispheres and the rear supporting leg is designed as a cuboid. The support force and drag resistance of different supporting legs are modeled and analyzed (it will be discussed detail in Section III-B), and the influence of different shapes of supporting legs on water jumping performance is analyzed (it will be discussed detail in Section V-A).

III. Force Analysis

The force analysis of the driving and supporting legs is the basis for dynamic modeling, however, the effects of water surface deformation on the driving and support forces are very complicated. In this section, we established an accurate driving force model based on Wagner's theory with the consideration of water surface deformation, and analyzed the support and resistance force of the robot with different postures.

A. Driving Force

The miniature water jumping robot adopts lightweight flat plate as driving leg, and the plate strikes the water surface at a certain speed and angle when the energy storage mechanism is released. To accurately analyze the forces exerted on the flat plate, we developed a force model for the oblique striking motion of the plate, as shown in Fig. 4. i) initial striking stage, the flat plate strikes water rapidly to push the stationary water, so that the water surface near the waterward side of plate rises and the backwater side is separated from the water to generate air cavity. ii) air cavity expansion stage, the waterward side of the flat plate is completely submerged, and the backwater side produces a larger air cavity. iii) air cavity collapse stage, the air cavity collapses rapidly under water pressure and covers the backwater side of the plate. iv) underwater striking stage, the air cavity vanishes completely. The complicated cavity and water surface deformation make it difficult to solve the driving force precisely. Wagner's theory [20], [21] takes into account the added mass and introduces a correction factor for the water surface deformation, and it can be applied when the effect of the air trapped between the driving leg and water surface is disregarded [22]. However, the driving leg strikes the water obliquely, so we modified the Wagner model by introducing added mass coefficient k_r and

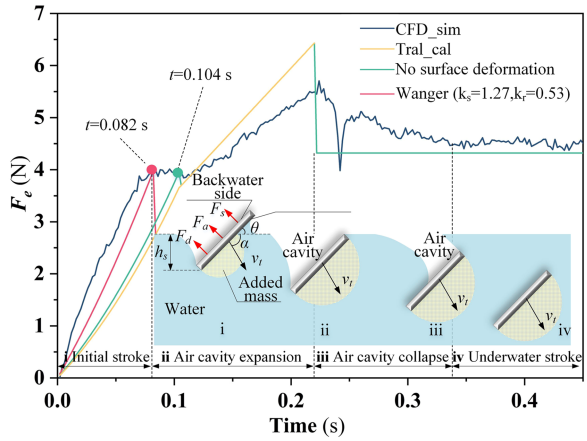

Fig. 4. Force simulation result of the flat plate with different calculation methods and air-water interface deformation. i. initial striking stage, ii. air cavity expansion, iii. air cavity collapse, and iv. underwater striking stage.

water surface deformation coefficient k_s. The fluid simulation method is used to solve these parameters, and we establish an accurate hydrodynamic model between driving legs and water.

The force $\boldsymbol{F_e}$ exerted on the flat plate mainly includes the added mass force $\boldsymbol{F_a}$, hydrostatic force $\boldsymbol{F_s}$ and hydrodynamic force $\boldsymbol{F_d}$, as shown in (1). m_a is the added mass of fluid, $\boldsymbol{v_t}$ is the striking velocity of plate, ρ is the water density, $\boldsymbol{g}$ is the acceleration of gravity, L is the plate length, h_s denotes the height of plate's lowest point to the water surface, θ indicates the angle between the flat plate and water surface, and C_d denotes the plate resistance coefficient. The added mass [23], [24], [25], [26], [27] is shown in the following:

$$\begin{cases} \boldsymbol{F_e} = \boldsymbol{F_a} + \boldsymbol{F_s} + \boldsymbol{F_d} \\ \boldsymbol{F_a} = d\left(m_a \boldsymbol{v_t}\right)/dt \\ \boldsymbol{F_s} = \rho \boldsymbol{g} L h_s^2/(2\sin\theta) \\ \boldsymbol{F_d} = C_d \rho h_s L \boldsymbol{v_t}^2/(2\sin\theta) \end{cases} \tag{1}$$

$$m_a = \frac{1}{2} k_r \rho \pi L \left(\frac{k_s h_s}{2\sin\theta}\right)^2. \tag{2}$$

The contact area between the plate and the water surface gradually increases in the water striking process, and the striking speed changes constantly, both factors will affect the added mass force. Therefore, $\boldsymbol{F_a}$ consists of two parts, one is the impact force $\boldsymbol{F_{am}}$ caused by the variation of contact area, and the other is the added mass force $\boldsymbol{F_{av}}$ caused by the variation of striking speed. The detailed solution procedure of $\boldsymbol{F_a}$ is shown in Appendix A, and the driving force can be calculated by (3) during the initial striking stage

$$\begin{aligned} &\boldsymbol{F_e} = \boldsymbol{F_{am}} + \boldsymbol{F_{av}} + \frac{\rho \boldsymbol{g} L h_s^2}{2\sin\theta} + \frac{C_d \rho h_s L \boldsymbol{v_t}^2}{2\sin\theta} \\ &h_s \leq W \sin\theta. \end{aligned} \tag{3}$$

When the waterward side of plate contacts with water surface completely, its submerged area will no longer change, $\boldsymbol{F_{am}}$ and k_s are 0 and 1, respectively. $\boldsymbol{F_e}$ can be calculated by (4) before the air cavity collapses, where T_c indicates the collapse time and

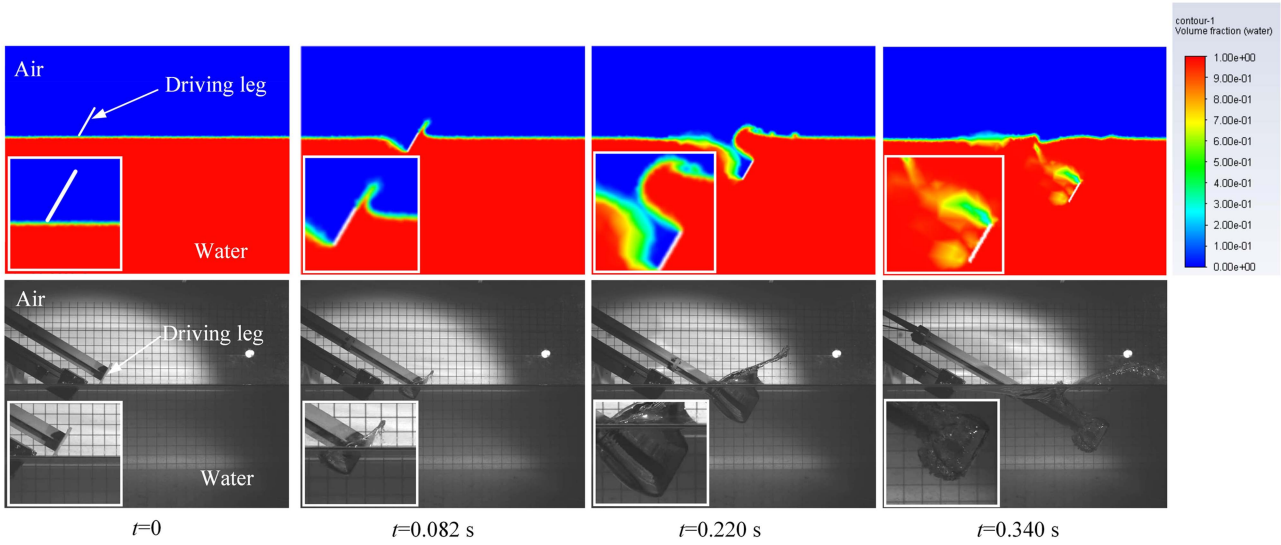

Fig. 5. Air–water interface deformation diagram during the flat plate striking water.

W denotes the plate width

$$\boldsymbol{F_e} = \frac{k_r \rho \pi L W^2 \dot{\boldsymbol{v}}_{\boldsymbol{t}}}{8} + \rho \boldsymbol{g} L W \left(h_s - \frac{W \sin\theta}{2} \right) + \frac{C_d \rho L W \boldsymbol{v}_{\boldsymbol{t}}^2}{2}$$

$$h_s > W \sin\theta, t \le T_c. \tag{4}$$

When the air cavity collapses, the backwater side of the plate is subjected to the impact force generated by water surface. Thereafter, the air cavity vanishes completely [28], [29], and the hydrostatic pressure on both sides of the plate is balanced when the plate thickness is ignored. $\boldsymbol{F_e}$ can be calculated by the following:

$$\boldsymbol{F_e} = \frac{k_r \rho \pi L W^2 \dot{\boldsymbol{v}}_{\boldsymbol{t}}}{8} + \frac{C_d \rho L W \boldsymbol{v}_{\boldsymbol{t}}^2}{2} \quad h_s > W \sin\theta, \; t \ge T_c. \tag{5}$$

The expansion and collapse of air cavity is affected by multifactors such as plate shape, inclination angle, and rowing velocity. In order to solve k_r and k_s precisely, we analyzed the forces on the flat plate at different striking velocities and striking angles, and carried out the two-phase fluid simulation with realistic physical parameters [30]. The computational domain size established in Fluent is 1000 mm × 1000 mm × 800 mm, the length, width, and thickness of the plate are 80, 60, and 2 mm, respectively, and θ is 60°. The areas where the plate contacts the fluid are set as boundary layer meshes, the plate and its surrounding boundary layers are set as dynamic mesh areas, and the meshes near the water–air interface are refined to improve the calculation accuracy. The motion speed is set to 1 m/s by the DEFINE_CG_MOTION macro. The calculation of the Weber number is shown in Appendix B (the Weber number is close to 1000), so the surface tension is not considered in the model due to the scale of the plate.

Fig. 4 shows the plate force curves obtained by CFD simulation results (CFD_sim), water pressure calculation method (Tral_cal), no consideration of water surface deformation ($k_s = 1, k_r = 0.62$), and Wagner model ($k_s = 1.27, k_r = 0.53$). k_s can be derived by linear fitting of CFD simulation results from 0 to 0.082 s and k_r can be calculated by (3). At the initial stroke stage, the impact force increases rapidly as the contact area between the plate and water surface increases. 0.082–0.22 s is the cavity expansion phase, as $\boldsymbol{F_a}$ and $\boldsymbol{v_t}$ are not changed, the plate is only subject to hydrostatic and dynamic pressure, and the force increases with the water penetration depth. 0.22–0.34 s is the air cavity collapse stage, the driving force drops sharply and then rises rapidly. It is because the collapsed liquid produces impact force on the backwater side of the plate, and the impact force will disappear when the backwater surface is completely covered by water. The duration time of the impact force is about 0.02 s, and it does not have a significant effect on the whole striking motion of the plate, so its effect is ignored in this article. Thereafter, the plate will be submerged completely and the hydrostatic pressure will vanish. Compared with other force calculation methods, the Wagner model ($k_s = 1.27$) can predict the force state of the plate in the initial striking stage more accurately, and it matches better with the fluid simulation results. Fig. 5 shows the simulation and experimental results of the air–water interface deformation during the water striking process, and the air cavity expansion and collapse process can be clearly observed.

The simulation results of T_c with different θ and $\boldsymbol{v_t}$, and the curves of k_r and k_s with different θ are shown in Fig. 6. T_c gradually increases as $\boldsymbol{v_t}$ decreases or θ increases, and T_c is larger when the striking speed is lower, it is because the penetration depth of air cavity generated by the low-speed striking is shallow, and the pressure on the air cavity is smaller. Equation (6) is the cubic polynomial fit to the mean value of T_c at different rowing speeds. k_r and k_s increase with θ, and k_r is approximately linear with θ. Linear and cubic polynomial fitting methods are used to establish k_r-θ and k_s-θ models, respectively, as shown in (7). Finally, the driving force model during the whole water striking process is derived

$$T_c = 9.32 \times 10^{-7}\theta^3 - 6.44 \times 10^{-5}\theta^2 + 2.09 \times 10^{-3}\theta + 0.126 \tag{6}$$

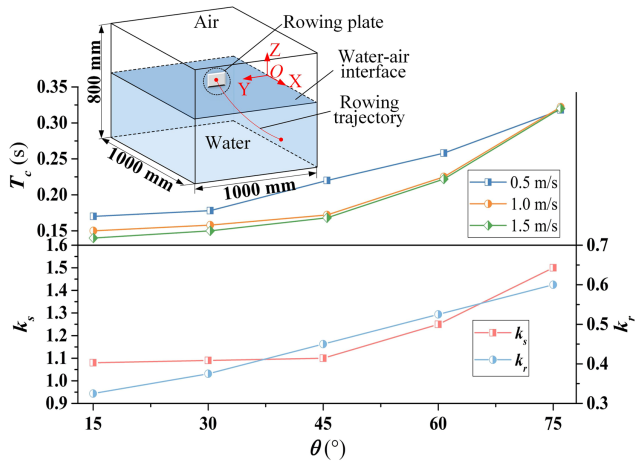

Fig. 6. Simulation result of T_c, k_r, and k_s with different rowing angles.

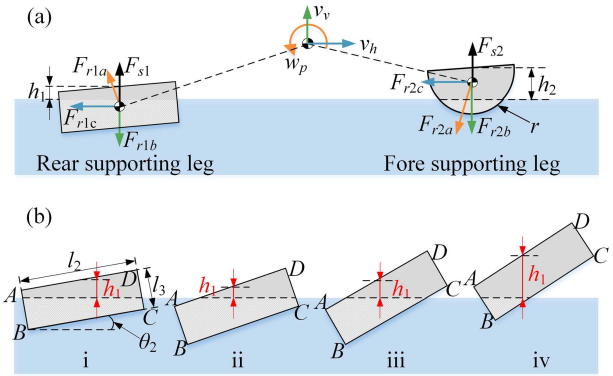

Fig. 7. Force analysis of the supporting legs with different postures. (a) Resistance and support force of supporting legs in each motion direction. (b) Different motion states of rear supporting leg during water jumping process.

$$\begin{cases} k_s = 2.46 \times 10^{-6}\theta^3 - 1.37 \times 10^{-4}\theta^2 + 2.06 \\ \qquad \times 10^{-3}\theta + 1.074 \\ k_r = 4.67 \times 10^{-3}\theta + 0.245. \end{cases} \tag{7}$$

B. Support and Resistance Force

When the supporting leg leaves the water surface, its contact area with water gradually decreases, resulting in a lower added mass force. Therefore, the supporting leg is mainly subjected to the hydrostatic pressure in the vertical direction and the drag resistance in the opposite direction of motion speed. The former is mainly determined by the volume of supporting leg submerged in water, and the latter is related to the drag coefficient, equivalent flow area, and robot motion speed. As shown in Fig. 7(a), we decompose the motion of the robot into three simple motions to analyze the resistance force: the flip motion around the centroid of robot, the vertical direction motion, and the horizontal direction motion. $\boldsymbol{F_{r1a}}$ and $\boldsymbol{F_{r2a}}$ are the resistance of the rear and fore supporting legs during the flip motion, $\boldsymbol{F_{r1b}}$ and $\boldsymbol{F_{r2b}}$ are the resistance during the vertical motion, and $\boldsymbol{F_{r1c}}$ and $\boldsymbol{F_{r2c}}$ are the resistance during the horizontal motion. H_1 and h_2 denote the distance from the rear and fore supporting leg to water surface, respectively, and r indicates the radius of the fore supporting leg. The resistance of supporting leg is shown in (8), where C_z denotes the water resistance coefficient. S_i is the equivalent resistance area of $\boldsymbol{F_i}$ ($i = r1a, r1b, r1c, r2a, r2b, r2c$), it is the projection area of the submerged part of supporting leg in the motion direction, l_{r1a} and l_{r2a} denote the lengths of the force arms from $\boldsymbol{F_{r1a}}$ and $\boldsymbol{F_{r2a}}$ to the centroid of robot, respectively. $\boldsymbol{v_v}$, $\boldsymbol{v_h}$, and ω_p are the vertical velocity, horizontal velocity, and pitch velocity of the robot, respectively

$$\begin{cases} \boldsymbol{F_{r1a}} = C_z\rho S_{r1a}(l_{r1a}\boldsymbol{\omega_p})^2/2, \boldsymbol{F_{r2a}} = C_z\rho S_{r2a}(l_{r2a}\boldsymbol{\omega_p})^2 \\ \boldsymbol{F_{r1b}} = C_z\rho S_{r1b}\boldsymbol{v_v^2}/2, \boldsymbol{F_{r2b}} = C_z\rho S_{r2b}\boldsymbol{v_v^2} \\ \boldsymbol{F_{r1c}} = C_z\rho S_{r1c}\boldsymbol{v_h^2}/2, \boldsymbol{F_{r2c}} = C_z\rho S_{r2c}\boldsymbol{v_h^2}. \end{cases} \tag{8}$$

Fig. 7(b) shows the different force states of the rear supporting leg, θ_2 indicates the pitch angle of the robot, l_1, l_2, and l_3 denote the length, width, and height of the rear supporting leg, respectively, and $\boldsymbol{F_{s1}}$ and $\boldsymbol{F_{s2}}$ indicate the support force of the rear and fore supporting legs, and they are segmented functions of h_1 and h_2. Points A, B, C, and D are the four vertices of the rectangular section of the rear supporting leg, and the height of these four points from water surface can describe its force state during the water jumping process. The detailed solution of $\boldsymbol{F_{s1}}$, S_{r1a}, and S_{r1b} is shown in Appendix C.

S_{r1c} can be calculated by (9) during the water jumping process. When $h_1 \geq 1/2l_2\sin\theta_2 + l_3\cos\theta_2$, the rear supporting leg is completely out of the water, and the support and resistance force disappear

$$S_{r1c} = l_1(l_3\cos\theta_2 + \frac{l_2\sin\theta_2}{2} - h_1). \tag{9}$$

For the fore supporting legs, when $0 \leq h_2 \leq r$, $\boldsymbol{F_{s2}}$ and S_i ($i = r2a, r2b, r2c$) can be calculated by (10). When $h_2 > r$, the fore supporting legs leave the water surface completely, and the support and resistance force disappear

$$\begin{cases} \boldsymbol{F_{s2}} = 2\rho\boldsymbol{g}\pi(\frac{2}{3}r^3 - r^2h_2 + \frac{h_2^3}{3}) \\ \boldsymbol{S_{r2a}} = \boldsymbol{S_{r2b}}\pi(r^2 - h_2^2) \\ \boldsymbol{S_{r2c}} = r^2a\cos(\frac{h_2}{r}) - h_2\sqrt{r^2 - h_2^2}. \end{cases} \tag{10}$$

IV. Water Jumping Dynamic Modeling and Driving Trajectory Optimization

Improving the accuracy of the robot dynamics model is the key to optimizing the structural parameters and improving the water jumping performance. Nevertheless, the output force of the energy storage mechanism, robot structure, and water surface deformation have complex effects on the robot's jumping motion. Consequently, we need to analyze the energy storage, force state, and robot posture during the whole water jumping process, and optimize the robot's structural parameters to improve the water jumping performance.

A. Dynamics Modeling

The hydrodynamic force model developed in Section III-A is derived in the condition of uniform speed motion. However, the rowing speed of the driving leg is varied during the water

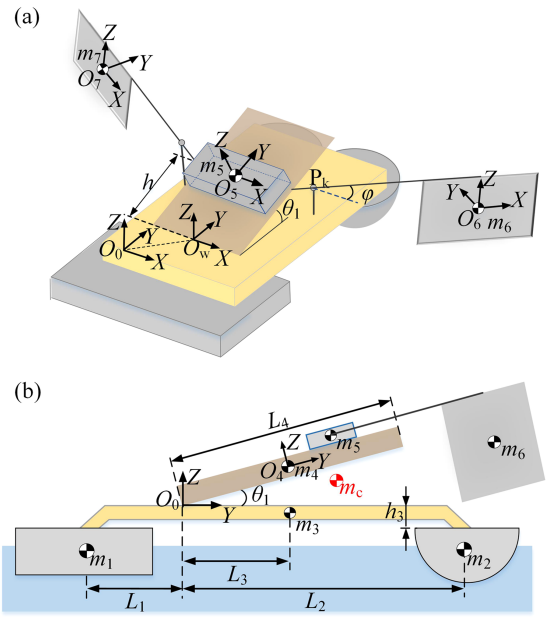

Fig. 8. Robot mass and size distribution.

jumping process. Moreover, the release speed of the energy storage mechanism and the motion attitude of the robot have complex effects on the rowing speed and swing angle of the driving legs. It increases the difficulty of solving the driving force accurately. Therefore, we first analyzed the influence of robot posture on the driving force.

Fig. 8 shows the mass and coordinate system of each part of the robot, m_i ($i = 1, 2, \ldots, 7$) denote the mass of the rear supporting leg, fore supporting legs, frame, energy storage mechanism, mobile slider, and two driving legs, respectively, and m_c denotes the centroid of the robot. The world coordinate system O_w and the robot's moving coordinate system O_0 are established at the intersection of the frame and the energy storage mechanism, and they have the same coordinate directions. The coordinate systems O_1, O_2, and O_3 are established at the centroid of the rear supporting leg, front supporting legs, and robot frame, respectively, and their coordinate directions are the same as O_0. The coordinate systems O_4 and O_5 are established at the centroid of the energy storage mechanism and the mobile slider, respectively, their *Y*-axes are parallel to plane *i* and *Z*-axes are perpendicular to plane *i*. The coordinate systems O_6 and O_7 are established at the centers of the driving legs on both sides, the length direction of the driving leg is the *X*-axis, the width direction is the *Z*-axis, and the *Y*-axis is perpendicular to the driving leg plane. Since the driving legs on both sides are symmetrically distributed, the right driving leg is selected for analysis in this article. The distances of O_1, O_2, and O_3 to the *Z*-axis of O_0 are L_1, L_2, and L_3, respectively, the length of the energy storage mechanism is L_4 and the height of the robot frame is h_3. The centroid position of the robot is ${}^{0}\mathbf{P}_{mc} = [x_c \quad y_c \quad z_c 1]^T$ in the O_0 coordinate system, and the detailed calculation of ${}^{0}\mathbf{P}_{mc}$ and rotational inertia J_x are shown in Appendix D.

The coordinate system O_c is established at the centroid position of the robot, and its coordinate direction is the same as O_0. The rowing speed is composed of two parts, one is the rowing speed ${}^{c}\boldsymbol{v_e}$ in the O_c coordinate system (the detailed calculation of ${}^{c}\boldsymbol{v_e}$ is shown in Appendix E), and the other is the motion speed of the O_c in the world coordinate system O_w, then the rowing speed of driving leg $\boldsymbol{v_e}$ can be calculated by (11). $\theta_2 = \int \boldsymbol{w_p}\, \mathrm{dt}$, $\theta_3 = a\tan({}^{c}z_6/{}^{c}y_6)$, where ${}^{c}y_6$ and ${}^{c}z_6$ are shown in Appendix E. α indicates the angle between the striking velocity and water surface, and it can be calculated by (12). θ will also change during the robot's water jumping process, and the detailed calculation is shown in Appendix F. Substituting $\boldsymbol{v_e}$, α, and θ into (1)–(7) enables accurate calculation of the driving force

$$\boldsymbol{v_e} = {}^{c}\boldsymbol{v_e} + \begin{bmatrix} 0 \\ \boldsymbol{v_h} \\ \boldsymbol{v_v} \end{bmatrix} + \boldsymbol{\omega_p}\sqrt{({}^{c}y_6)^2 + ({}^{c}z_6)^2} \times \begin{bmatrix} 0 \\ -s(\theta_2+\theta_3) \\ c(\theta_2+\theta_3) \end{bmatrix} = \begin{bmatrix} \boldsymbol{v_{ex}} \\ \boldsymbol{v_{ey}} \\ \boldsymbol{v_{ez}} \end{bmatrix} \tag{11}$$

$$\alpha = a\tan\left(\boldsymbol{v_{ez}} \Big/ \sqrt{\boldsymbol{v_{ex}^2} + \boldsymbol{v_{ey}^2}}\right). \tag{12}$$

The robot adopts Ten—Tor energy storage mechanism, and the output force $\boldsymbol{F_j}$ is shown in (13). The dynamic model between energy storage mechanism and driving legs is shown in (14), where $\dot{\boldsymbol{h}}$ and $\ddot{\boldsymbol{h}}$ denote the velocity and acceleration of the energy storage mechanism, $\dot{\boldsymbol{w}}_{\boldsymbol{l}}$ and l denote the angular acceleration and length of driving legs, respectively, J_l denotes the rotational inertia of the driving leg around the point P_k

$$\boldsymbol{F_j} = hk_1\left(\frac{l_{cd}-x_1}{\sqrt{4l_{bc}^2-h^2}}+1\right) + \frac{4l_{bc}k_3}{l_{ab}\sqrt{4l_{bc}^2-h^2}} \times \left(\psi_3 - a\cos\frac{\sqrt{4l_{bc}^2-h^2}}{2l_{bc}}\right) \tag{13}$$

$$\begin{cases} \ddot{\boldsymbol{h}} = \frac{1}{m_5}\left(\boldsymbol{F_j} - 2\frac{F_e l + J_l \dot{\boldsymbol{w}}_{\boldsymbol{l}}}{d_0}\right) \\ \dot{\boldsymbol{w}}_{\boldsymbol{l}} = \frac{d_0\ddot{\boldsymbol{h}}}{d_0^2+(d_1-h)^2} + \frac{2d_0(d_1-h)\dot{\boldsymbol{h}}}{\left[d_0^2+(d_1-h)^2\right]^2} \\ d_0 = \frac{l_{ab}+l_{bc}}{\tan\varphi_0+\tan\varphi_1},\ d_1 = \frac{l_{ab}+l_{bc}}{\tan\varphi_0+\tan\varphi_1}\tan\varphi_0. \end{cases} \tag{14}$$

Equation (14) illustrates the relationship between the motion of energy storage mechanism and driving force. Moreover, the driving force is also influenced by the robot's posture. To further optimize the jumping performance, we analyze the whole water jumping process of the robot, as shown in Fig. 9. i) floating stage, the robot floats on the water surface with front and rear supporting forces $\boldsymbol{F_{s2}}, \boldsymbol{F_{s1}}$ and gravity $\boldsymbol{G}$. ii) initial rowing stage, the robot pitches under the driving force $\boldsymbol{F_q}$ with a pitch angle of θ_2, the drag resistance of fore and rear supporting legs are $\boldsymbol{F_{r2}}, \boldsymbol{F_{r1}}$ respectively. iii) fore supporting leg and water surface disappears completely. iv) rear supporting leg leaving water stage ($h_1 > l_2 \sin\theta_2/2 + l_3 \cos\theta_2$), the force between the rear supporting leg and water surface disappears, and the robot is only subject to the driving force and gravity. The dynamics model of

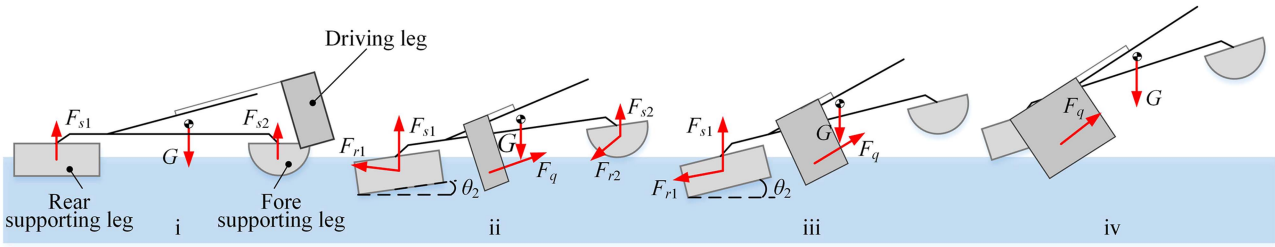

Fig. 9. Whole water jumping process of the robot.

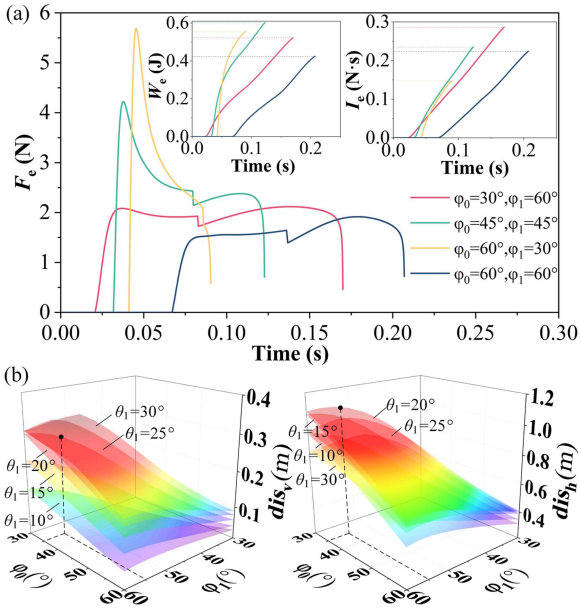

Fig. 10. Effects of driving trajectory on the water jumping performance. (a) F_e, W_e, and I_e with different swing angles and tilt angles. (b) Effects of φ_0, φ_1, and θ_1 on the water jumping height. (c) Effects of φ_0, φ_1, and θ_1 on the water jumping distance.

the robot for the whole water jumping process is shown in (15), where $\boldsymbol{F_q}$ is the projection of $\boldsymbol{F_e}$ in the Y-axis direction of the coordinate system O_4 ($\boldsymbol{F_q} = 2\boldsymbol{F_e}d_0/\sqrt{d_0^2 + (d_1 - h)^2}$), $l_i(l_j)$ denotes the arm of force from $\boldsymbol{F_i}$ ($\boldsymbol{F_j}$) to the centroid of robot, θ_2 and $\ddot{\boldsymbol{\theta}}_{\boldsymbol{2}}$ denote the pitch angle and angular acceleration of the robot, θ_4 and θ_5 are intermediate variables, $\boldsymbol{a_v}$ and $\boldsymbol{a_h}$ are the acceleration in vertical and horizontal directions, respectively

$$\begin{cases} \sum \boldsymbol{F_i} l_i - \sum \boldsymbol{F_j} l_j = J_x \ddot{\boldsymbol{\theta}}_{\boldsymbol{2}} (i = q, s2, r1b, \\ \quad j = s1, r1a, r2a, r2b, r1c, r2c) \\ \boldsymbol{F_q} \sin(\theta_1 + \theta_2) + \boldsymbol{F_{s1}} + \boldsymbol{F_{s2}} + \boldsymbol{F_{r1a}} \cos(\theta_2 + \theta_4) \\ \quad -[\boldsymbol{F_{r2a}} \cos(\theta_5 - \theta_2) + \boldsymbol{F_{r1b}} + \boldsymbol{F_{r2b}} + \boldsymbol{G}] = m\boldsymbol{a_v} \\ \boldsymbol{F_q} \cos(\theta_1 + \theta_2) - [\boldsymbol{F_{r1a}} \sin(\theta_2 + \theta_4) \\ \quad + \boldsymbol{F_{r2a}} \sin(\theta_5 - \theta_2) + \boldsymbol{F_{r1c}} + \boldsymbol{F_{r2c}}] = m\boldsymbol{a_h} \\ \theta_4 = \text{atan}\frac{z_c + h_3 + \frac{l_3}{2}}{L_1 + y_c}, \theta_5 = \text{atan}\frac{z_c + h_3 + \frac{3}{8}r}{L_2 - y_c}. \end{cases} \tag{15}$$

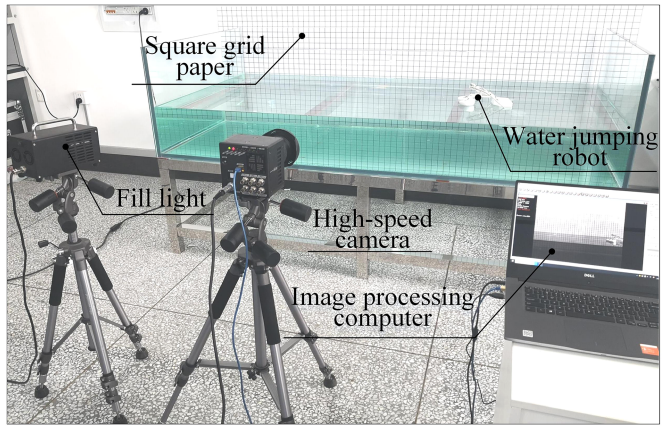

Fig. 11. Experimental setup for robot's water jumping motion.

B. Driving Trajectory Optimization

The rowing trajectory has decisive effects on the swing range, rowing depth and force state of the driving legs, which is also an important factor affecting the force and work during the rowing process. In our previous work [31], we improved the driving force and work by optimizing the spatial rowing trajectory of driving legs, which enhanced the motion speed of the robot. Therefore, we analyze the effects of rowing trajectory parameters on driving force, work and water jumping performance based on the dynamic model in Section IV-A.

The swing angles φ_0, φ_1 of driving leg and the inclination angle θ_1 of the energy storage mechanism are important parameters to determine the rowing trajectory. φ_0 and φ_1 affect the height of the driving leg to the water surface and the rowing trajectory length, respectively. θ_1 affects the components of the driving force in the vertical and horizontal directions. We select four combinations of swing angles to compare $\{\varphi_0 = 30°, \varphi_1 = 60°\}$, $\{\varphi_0 = \varphi_1 = 45°\}$, $\{\varphi_0 = 60°, \varphi_1 = 30°\}$, $\{\varphi_0 = \varphi_1 = 60°\}$, and analyze the influence of swing angle on the driving force, work and impulse. It is assumed that the dimensions of the robot do not exceed 0.45 m, the total mass does not exceed 95 g, $l = 0.2$ m. $L = 0.08$ m, $W = 0.06$ m, the thickness of the plate $T_h = 0.002$ m, $L_1 = 0.06$ m, $L_2 = 0.1$ m, $L_3 = 0.02$ m, $L_4 = 0.08$ m. The dimensions of the supporting leg are as follows: $l_1 = 0.08$ m, $l_2 = 0.05$ m, $l_3 = 0.012$ m, $r = 0.025$ m, and the mass of each part of the robot is as follows: $m_1 = 9$ g, $m_2 = 6.5$ g, $m_3 = 10$ g, $m_4 = 42$ g, $m_5 = 1.2$ g, $m_6 = 8$ g, so $J_l = m_6(L^2 + T_h^2)/12 + m_6 l^2 = 3.24 \times 10^{-4}$ kg·m^2. When

$\theta_1 = 20°$, the driving force F_e for different swing angle parameters is calculated by (1), (2), (11)–(15). The integral of the product of $\boldsymbol{F_e}$ and the rowing trajectory length is W_e, and the integral of the product of $\boldsymbol{F_e}$ and the rowing time is I_e. As shown in Fig. 10(a), when $\varphi_0 = 30°$, $\varphi_1 = 60°$, the rowing time of the driving leg is the longest, and the impulse is the largest. When $\varphi_0 = 60°$, $\varphi_1 = 30°$, the instantaneous driving force is the largest, but the rowing time is the shortest, and the impulse is the smallest. When $\varphi_0 = \varphi_1 = 45°$, the work of the driving leg is the largest, and when $\varphi_0 = \varphi_1 = 60°$, the driving force and work are minimum.

To further analyze the effect of φ_0, φ_1, θ_1 on the water jumping performance, the instantaneous velocities $\boldsymbol{v_v}$ and $\boldsymbol{v_h}$ when the robot leaves water surface are calculated by integrating the $\boldsymbol{a_v}$ and $\boldsymbol{a_h}$ solved by (15), so the jumping distances dis_v and jumping height dis_h ($\text{dis}_v = \boldsymbol{v_v^2}/(2\boldsymbol{g})$, $\text{dis}_h = 2\boldsymbol{v_h v_v}/\boldsymbol{g}$) are obtained. The analysis results are shown in Fig. 10(b) and (c). dis_v gradually increases with θ_1, but the growth rate slows down. As θ_1 increases, dis_h increases first and then decreases, and the horizontal jumping distance is the farthest when $\theta_1 = 20°$. If $\theta_1 < 15°$, dis_v and dis_h increase as φ_0 decreases or φ_1 increases, and when $\theta_1 > 15°$, dis_v and dis_h increase and then decrease as φ_1 increases. When $\varphi_0 = 35°$ and $\varphi_1 = 55°$, the maximum dis_h is 1.07 m and dis_v is 0.28 m.

V. Water Jumping Experiment

A. Different Supporting Legs Shapes

The experimental platform of water jumping motion is shown in Fig. 11, which mainly includes a transparent glass tank (2 m × 1 m × 0.5 m), a high-speed camera, an image processing computer, a square grid paper (the size of the square grid cell is 30 mm × 30 mm), and the water jumping robot. The high speed camera records the whole water jumping process of the robot at 500 frames/s. The supporting legs with different shapes are also important factors affecting the water jumping performance. In the initial rowing stage, the fore supporting legs are separated from water surface first, so the drag resistance should be minimized to enable the robot reach a suitable jumping angle. When the fore supporting legs are completely separated from water surface, the weight of robot and the inertial moment generated by pitching motion are all exerted on the rear supporting leg and driving legs, so the rear supporting leg is required to provide sufficient support force to prevent the robot from overturning.

Three different supporting legs shapes (hemisphere–hemisphere, hemisphere–cuboid, and cuboid–cuboid) are designed for comparison, and the robot jumping trajectory can be derived according to (15). Fig. 12(a) shows the experimental and theoretical results of the jumping motion with different supporting leg shapes. Although the cuboid–cuboid supporting system is capable of water jumping, the jumping height is only 106 mm, and the jumping height is 243 mm when the fore and rear supporting legs are hemisphere-cuboid. It is because the drag resistance of the hemispherical supporting leg is lower, which is more conducive to the jumping posture adjustment. Fig. 12(a) also shows the water jumping state of the hemisphere and cuboid rear supporting leg respectively. The former overturned because

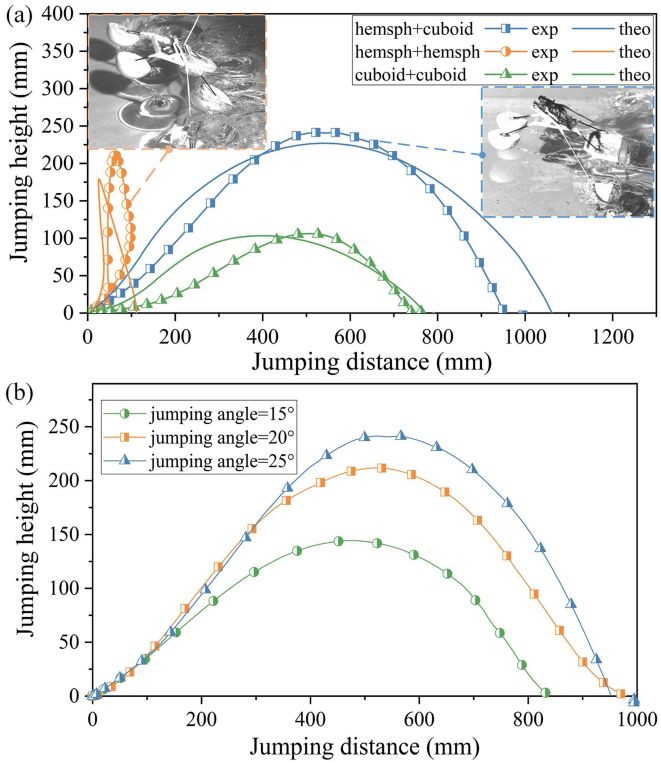

Fig. 12. Water jumping experiments of the miniature robot. (a) Robot jumping trajectory with different supporting legs shapes. (b) Robot jumping trajectory with different jumping angles. (c) Snapshots of the water jumping motion.

the resistance area of the hemispherical supporting leg is small and it is susceptible to sink under the pitching impact, while the resistance area of cuboid rear supporting leg is larger and it can resist the pitching impact. Therefore, the hemisphere-cuboid supporting system is more favorable to improve water jumping performance. The experimental results are consistent with the theory, and the error may be caused by two main factors. 1) The flow resistance coefficient of the driving legs and supporting legs are not accurate enough. 2) The transmission gap in the driving mechanism reduces the water jumping speed.

B. Different Jumping Angles

The pitch attitude of the robot can be changed by adjusting the angle between energy storage mechanism and robot frame. Fig. 12(b) shows the jumping trajectory of the robot with hemisphere-cuboid supporting legs at different pitch angles. As the pitch angle increases, the jumping height gradually increases and the jumping distance first increases and then decreases. The maximum jumping height and distance are 241 and 976 mm, respectively, and the corresponding pitch angles are 25° and 20°. When the pitch angle exceeds 25°, the vertical component of the driving force is larger and the horizontal component is smaller, which reduces the jumping distance and makes it more susceptible to overturning. When the pitch angle is 25°, the water jumping motion is shown in Fig. 13. The energy storage process of the hexagonal rod mechanism takes 5.7 s, and the maximum jumping height and distance are 241 and 965 mm, respectively.

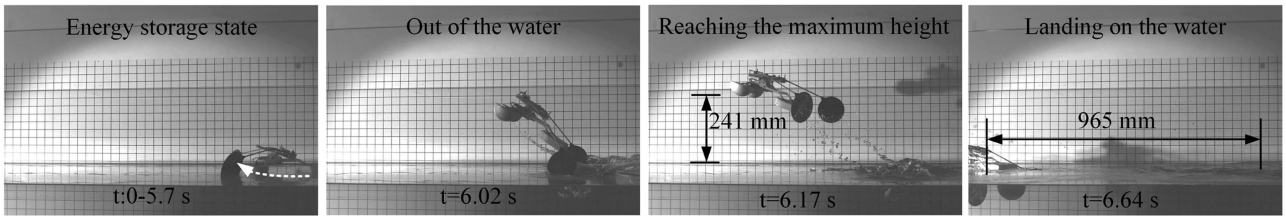

Fig. 13. Snapshots of the water jumping motion.

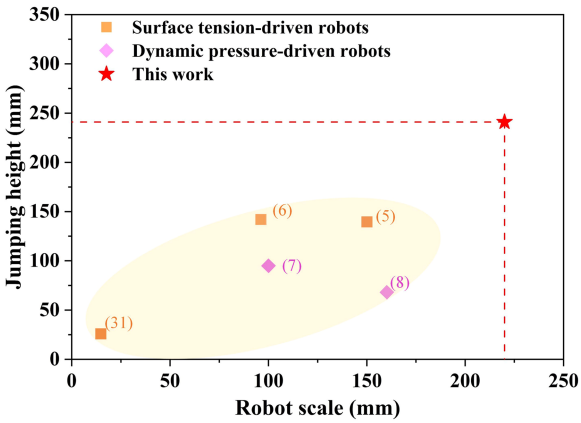

Fig. 14. Jumping performance comparison of existing water jumping robots.

Fig. 14 shows the motion performance comparison of the existing water jumping robots, and the robot designed in this article has a higher jumping height. The jumping distance/body length ratio reaches 4.4, which is 1.88 times higher than that of the robot we developed in 2012 [5].

VI. Conclusion

This article established the force model of rectangular driving legs with different striking angles and velocities based on the modified Wagner theory. It improved the solution accuracy of the interaction force between the robot and water–air interface. The dynamic characteristics of water jumping process affected by multifactors such as energy storage mechanism, rowing trajectory, and supporting legs shape were analyzed in detail. The miniature water jumping robot is optimized and designed based on the dynamic analysis of the whole water jumping process. The fabricated robot weighs 91 g and its length, width, and height are 220, 410, and 95 mm, respectively.

We improved the energy storage capacity and output force by optimizing the energy storage mechanism size and element type, and selected the Ten–Tor energy storage mechanism, and established the dynamic model of the whole water jumping process with consideration of robot's posture. The water jumping performance was optimized by analyzing the effects of the rowing trajectory parameters (swing angle range, driving mechanism inclination angle) on the driving force, work, and impulse. Finally, the water jumping experiments with different supporting leg shapes and jumping angles were carried out, and the hemisphere-cuboid supporting leg layout was favorable to the water jumping performance. As the pitch angle increases, the jumping height gradually increases and the jumping distance first increases and then decreases. When φ_0, φ_1, and θ_1 are 35°, 55°, and 25°, respectively, the water jumping height and distance reach 241 and 965 mm, and the jumping height/body length ratio and jumping distance/body length ratio reach 1.1 and 4.4, respectively, which is better than other miniature water-jumping robots according to the literature that we have retrieved so far.

In the follow-up study, we will design a miniature robot with both water sliding and jumping abilities, and the two movement modes can be switched automatically. The jumping performance will be further improved by the optimization of the shape and area of the driving legs. In the future, this robot will be able to cross small obstacles and waves, and it can be used for water surface reconnaissance and water quality monitoring when equipped with miniature cameras and communication modules. In addition, it is suitable for networking to build underwater navigation and relay nodes due to its small scale and stealthiness.

Appendix A

The added mass force $\boldsymbol{F_a}$ is the change in fluid momentum generated during the water striking process, which is determined by the added mass $m_a(t)$ and the striking velocity $\boldsymbol{v_t}(t)$

$$\boldsymbol{F_a} = \frac{d}{dt}\left[m_a(t)\boldsymbol{v_t}(t)\right] = \frac{dm_a(t)}{dt}\boldsymbol{v_t}(t) + \frac{d\boldsymbol{v_t}(t)}{dt}m_a(t). \tag{16}$$

The former is the impact force $\boldsymbol{F_{am}}$, and the latter is the added mass force $\boldsymbol{F_{av}}$ caused by the change of striking speed, which is related to the plate acceleration

$$\begin{cases} \frac{dm_a(t)}{dt} = \frac{d}{dt}\left[\frac{1}{2}k_r\rho\pi L\left(\frac{k_s h_s(t)}{2\sin\theta}\right)^2\right]\frac{k_r k_s^2\rho\pi L h_s(t)}{4\sin^2\theta}\frac{dh_s(t)}{dt} \\ \frac{dh_s(t)}{dt} = |\boldsymbol{v_t}(t)|\sin\alpha. \end{cases} \tag{17}$$

$\boldsymbol{F_{am}}$ and $\boldsymbol{F_{av}}$ are as follows, where α indicates the angle between the striking velocity and water surface. α will change during the robot's water jumping process, and it can be calculated by (12)

$$\begin{cases} \boldsymbol{F_{am}} = \frac{k_r k_s^2\rho\pi L h_s \boldsymbol{v_t}^2\sin\alpha}{4\sin^2\theta} \\ \boldsymbol{F_{av}} = \frac{k_r k_s^2\rho\pi L h_s^2\dot{\boldsymbol{v}}_{\boldsymbol{t}}}{8\sin^2\theta}. \end{cases} \tag{18}$$

Appendix B

The calculation of the Weber number can clarify whether surface tension is important for the driving force. The length and

width of the flat plate are 80 and 60 mm, and its characteristic dimension L can be calculated by (19), where S is the area of the flat plate submerged in water and C is the perimeter of the plate.

$$L = 4 \times \frac{S}{C} = 4 \times \frac{60 \times 80}{2 \times (60 + 80)} \approx 68.57mm. \tag{19}$$

The characteristic size of the flat plate L is 0.0686 m, and the Weber number is calculated by (20) when the striking speed is 1 m/s, where ρ is the fluid density, and σ is the surface tension coefficient

$$\text{Weber} = \frac{\rho v^2 L}{\sigma} = \frac{1 \times 10^3 \times 1^2 \times 6.857 \times 10^{-2}}{7.28 \times 10^{-2}} \approx 942. \tag{20}$$

Appendix C

When points A, D are above the water surface and points B, C are below the water surface, as shown in Fig. 7(b) subplots i, $1/2l_2\sin\theta_2 \le h_1 \le l_3\cos\theta_2 – 1/2l_2\sin\theta_2$. S_{r1a} and S_{r1b} are almost equal when the angle between $\boldsymbol{F_{s1}}$ and $\boldsymbol{F_{r1a}}$ is small. $\boldsymbol{F_{s1}}$, S_{r1a}, and S_{r1b} can be calculated as follows:

$$\begin{cases} \boldsymbol{F_{s1}} \rho g l_1 l_2 (l_3 - \frac{h_1}{\cos\theta_2}) \\ S_{r1a} = S_{r1b} = \left[(l_3 \cos\theta_2 + \frac{l_2}{2} \sin\theta_2 - h_1) \tan\theta_2 \right. \\ \left. + l_2 \cos\theta_2 \right] l_1. \end{cases} \tag{21}$$

When point D is above the water surface and points A, B, C are below the water surface, as shown in Fig. 7(b) subplots ii, $h_1 \le 1/2l_2\sin\theta_2$ and $h_1 \le l_3\cos\theta_2 – 1/2l_2\sin\theta_2$. $\boldsymbol{F_{s1}}$, S_{r1a}, and S_{r1b} can be calculated as follows:

$$\begin{cases} \boldsymbol{F_{s1}} \rho g l_1 \left[l_2 l_3 - \frac{\tan\theta_2}{2} \left(\frac{l_2}{2} + \frac{h_1}{\sin\theta_2} \right)^2 \right] \\ S_{r1a} = S_{r1b} = (l_3 \sin\theta_2 + l_2 \cos\theta_2) l_1. \end{cases} \tag{22}$$

When points C, D are above the water surface and points A, B are below the water surface, as shown in Fig. 7(b) subplots iii, $l_3\cos\theta_2 – 1/2l_2\sin\theta_2 \le h_1 \le ½l_2\sin\theta_2$. $\boldsymbol{F_{s1}}$, S_{r1a}, and S_{r1b} can be calculated as follows:

$$\begin{cases} \boldsymbol{F_{s1}} \frac{1}{2} \rho g l_1 l_3 (l_2 - \frac{2h_1}{\sin\theta_2} + \frac{l_3}{\tan\theta_2}) \\ S_{r1a} = S_{r1b} = \left[l_3 \sin\theta_2 + \frac{1}{\tan\theta_2} (l_3 \cos\theta_2 \right. \\ \left. + \frac{l_2}{2} \sin\theta_2 - h_1) \right] l_1. \end{cases} \tag{23}$$

When the robot is about to leave the water surface, the force state of the rear supporting leg is shown in subplot iv, $l_3\cos\theta_2 – 1/2l_2\sin\theta_2 \le h_1$, and $1/2l_2\sin\theta_2 \le h_1 \le 1/2l_2\sin\theta_2 + l_3\cos\theta_2$. $\boldsymbol{F_{s1}}$, S_{r1a}, and S_{r1b} can be calculated as follows:

$$\begin{cases} \boldsymbol{F_{s1}} \frac{1}{2} \rho g l_1 (l_3 - \frac{h_1}{\cos\theta_2} + \frac{l_2}{2} \tan\theta_2)(\frac{l_2}{2} - \frac{h_1}{\sin\theta_2} + \frac{l_3}{\tan\theta_2}) \\ S_{r1a} = S_{r1b} = (l_3 \cos\theta_2 + \frac{l_2}{2} \sin\theta_2 – h_1)(\tan\theta_2 + \frac{1}{\tan\theta_2}) l_1. \end{cases} \tag{24}$$

Appendix D

The homogeneous transformation matrix of O_i ($i = 1, 2, \ldots, 6$) in the coordinate system O_0 are ${}^0\mathbf{T}_i$

$${}^0\mathbf{T}_1 = \begin{bmatrix} 1 & 0 & 0 & 0 \\ 0 & 1 & 0 & -L_1 \\ 0 & 0 & 1 & -(l_3/2 + h_3) \\ 0 & 0 & 0 & 1 \end{bmatrix}$$

$${}^0\mathbf{T}_2 = \begin{bmatrix} 1 & 0 & 0 & 0 \\ 0 & 1 & 0 & L_2 \\ 0 & 0 & 1 & -(3r/8 + h_3) \\ 0 & 0 & 0 & 1 \end{bmatrix}$$

$${}^0\mathbf{T}_3 = \begin{bmatrix} 1 & 0 & 0 & 0 \\ 0 & 1 & 0 & L_3 \\ 0 & 0 & 1 & -h_3/2 \\ 0 & 0 & 0 & 1 \end{bmatrix}$$

$${}^0\mathbf{T}_4 = \begin{bmatrix} 1 & 0 & 0 & 0 \\ 0 & c\theta_1 & -s\theta_1 & c\theta_1 L_4/2 \\ 0 & s\theta_1 & c\theta_1 & s\theta_1 L_4/2 \\ 0 & 0 & 0 & 1 \end{bmatrix}$$

$${}^0\mathbf{T}_5 = \begin{bmatrix} 1 & 0 & 0 & 0 \\ 0 & c\theta_1 & -s\theta_1 & hc\theta_1 \\ 0 & s\theta_1 & c\theta_1 & hs\theta_1 \\ 0 & 0 & 0 & 1 \end{bmatrix}$$

$${}^5\mathbf{T}_6 = Tran(l_{hg}/2 + d_0, d_1 - h, 0) R(Z, \varphi) Tran(l, 0, -W/2)$$

$$= \begin{bmatrix} c\varphi & -s\varphi & 0 & l_{hg}/2 + d_0 + lc\varphi \\ s\varphi & c\varphi & 0 & d_1 - h + ls\varphi \\ 0 & 0 & 1 & -W/2 \\ 0 & 0 & 0 & 1 \end{bmatrix}$$

$${}^0\mathbf{T}_6 = {}^0\mathbf{T}_5 \cdot {}^5\mathbf{T}_6$$

$$= \begin{bmatrix} c\varphi & -s\varphi & 0 & lc\varphi + l_{hg}/2 + d_0 \\ c\theta_1 s\varphi & c\theta_1 c\varphi & -s\theta_1 & c\theta_1(ls\varphi + d_1) + s\theta_1 W/2 \\ s\theta_1 s\varphi & s\theta_1 c\varphi & c\theta_1 & s\theta_1(ls\varphi + d_1) - c\theta_1 W/2 \\ 0 & 0 & 0 & 1 \end{bmatrix} \tag{25}$$

where $s\varphi$, $c\varphi$, $s\theta_1$, and $c\theta_1$ denote $\sin\varphi$, $\cos\varphi$, $\sin\theta_1$, and $\cos\theta_1$, respectively. $\sin\varphi$ and $\cos\varphi$ can be calculated as follows:

$$\begin{cases} \sin\varphi = (d_1 - h)/\sqrt{d_0^2 + (d_1 - h)^2} \\ cos\varphi = d_0/\sqrt{d_0^2 + (d_1 - h)^2}. \end{cases} \tag{26}$$

The centroid position of each component of the robot in the O_0 coordinate system is ${}^0\mathbf{P}_{mi} = {}^0\mathbf{T}_i [0 \;\; 0 \;\; 0 \;\; 1]^T = [x_i y_i z_i 1]^T$ ($i = 1, 2, \ldots, 7$), and the centroid position ${}^0\mathbf{P}_{mc}$ and the

$$^{w}\mathbf{R_6} = \begin{bmatrix} c\varphi & -s\varphi & 0 \\ s\varphi(c\theta_1 c\theta_2 - s\theta_1 s\theta_2) & c\varphi(c\theta_1 c\theta_2 - s\theta_1 s\theta_2) & -c\theta_1 s\theta_2 - s\theta_1 c\theta_2 \\ s\varphi(c\theta_1 s\theta_2 + s\theta_1 c\theta_2) & c\varphi(c\theta_1 s\theta_2 + s\theta_1 c\theta_2) & c\theta_1 c\theta_2 - s\theta_1 s\theta_2 \end{bmatrix}.$$

rotational inertia J_x of the robot can be calculated as follows:

$$\begin{cases} ^{0}\mathbf{P_{mc}} = \frac{1}{m}\sum_{i=1}^{7} m_i [x_i \quad y_i \quad z_i \quad 1]^T \\ = [x_c \quad y_c \quad z_c \quad 1]^{\mathrm{T}}, m = \sum_{i=1}^{7} m_i \\ J_x = \sum_{i=1}^{7} \left[(y_i - y_c)^2 + (z_i - z_c)^2\right] m_i. \end{cases} \tag{27}$$

APPENDIX E

$^{c}\mathbf{T_6}$ indicates the position of the coordinate system O_6 in the O_c coordinate system.

$$^{c}\mathbf{T_6} = {}^{c}\mathbf{T_0} \cdot {}^{0}\mathbf{T_6} = \begin{bmatrix} c\varphi & -s\varphi & 0 & ^{c}x_6 \\ c\theta_1 s\varphi & c\theta_1 c\varphi & -s\theta_1 & ^{c}y_6 \\ s\theta_1 s\varphi & s\theta_1 c\varphi & c\theta_1 & ^{c}z_6 \\ 0 & 0 & 0 & 1 \end{bmatrix} \tag{28}$$

where

$$\begin{cases} ^{c}x_6 = lc\varphi + l_{hg}/2 + d_0 \\ ^{c}y_6 = c\theta_1(ls\varphi + d_1) + s\theta_1 W/2 - y_c \\ ^{c}z_6 = s\theta_1(ls\varphi + d_1) - c\theta_1 W/2 - z_c. \end{cases}$$

The rowing speed of the driving leg $\boldsymbol{v_e}$ is along the negative direction of the *Y*-axis of the coordinate system O_6, and $\boldsymbol{v_e}$ is denoted as $^{c}\boldsymbol{v_e}$ in the O_c coordinate system. It is written as follows:

$$^{c}\boldsymbol{v_e} = \boldsymbol{\omega_l} l \begin{bmatrix} c\varphi & -s\varphi & 0 \\ c\theta_1 s\varphi & c\theta_1 c\varphi & -s\theta_1 \\ s\theta_1 s\varphi & s\theta_1 c\varphi & c\theta_1 \end{bmatrix} \begin{bmatrix} 0 \\ -1 \\ 0 \end{bmatrix} = \boldsymbol{\omega_l} l \begin{bmatrix} s\varphi \\ -c\theta_1 c\varphi \\ -s\theta_1 c\varphi \end{bmatrix} \tag{29}$$

ω_l indicates the rotation speed of the driving leg around the point P_k.

APPENDIX F

$^{w}\mathbf{T_6}$ indicates the position of the coordinate system O_6 in the O_w coordinate system

$$^{w}\mathbf{T_6} = {}^{w}\mathbf{T_0} \cdot {}^{0}\mathbf{T_6} = \begin{bmatrix} & & & ^{c}x_6 \\ & ^{w}\mathbf{R_6} & & Y + (^{c}y_6 + y_c)c\theta_2 - (^{c}z_6 + z_c)s\theta_2 \\ & & & Z + (^{c}z_6 + z_c)c\theta_2 + (^{c}y_6 + y_c)s\theta_2 \\ 0 & 0 & 0 & 1 \end{bmatrix} \tag{30}$$

where unnumbered equation shown at the top of this page, $Y = \int \boldsymbol{v_h}\, \mathrm{d}t$, $Z = \int \boldsymbol{v_v}\, \mathrm{d}t$, $^{w}\mathbf{P_e}$ denotes the direction vector of the *Y*-axis of the O_6 coordinate system in the O_w coordinate system. It can be calculated as follows:

$$^{w}\mathbf{P_e} = {}^{w}\mathbf{R_6} \begin{bmatrix} 0 \\ 1 \\ 0 \end{bmatrix} \begin{bmatrix} -s\varphi \\ c\varphi(c\theta_1 c\theta_2 - s\theta_1 s\theta_2) \\ c\varphi(c\theta_1 s\theta_2 + s\theta_1 c\theta_2) \end{bmatrix} = \begin{bmatrix} ^{w}\mathbf{p_{ex}} \\ ^{w}\mathbf{p_{ey}} \\ ^{w}\mathbf{p_{ez}} \end{bmatrix} \tag{31}$$

the angle θ between the driving leg and water surface is as follows:

$$\theta = a\tan\left(\sqrt{^{w}\mathbf{p}_{ex}^2 + {}^{w}\mathbf{p}_{ey}^2} / {}^{w}\mathbf{p_{ez}}\right). \tag{32}$$

REFERENCES

[1] M. M. Plecnik, D. W. Haldane, J. K. Yim, and R. S. Fearing, "Design exploration and kinematic tuning of a power modulating jumping monopod," *J. Mech. Robot.*, vol. 9, no. 1, Feb. 2017, Art. no. 011009.

[2] J. Zhao et al., "MSU jumper: A single-motor-actuated miniature steerable jumping robot," *IEEE Trans. Robot.*, vol. 29, no. 3, pp. 602–614, Jun. 2013.

[3] F. Li et al., "Jumping mini-robot with bio-inspired legs," in *Proc. IEEE Int. Conf. Robot. Biomimetics*, 2009, pp. 933–938.

[4] M. Kovac, M. Fuchs, A. Guignard, J. C. Zufferey, and D. Floreano, "A miniature 7G jumping robot," in *Proc. IEEE Int. Conf. Robot. Automat.*, 2008, pp. 373–378.

[5] J. Zhao, X. Zhang, N. Chen, and Q. Pan, "Why superhydrophobicity is crucial for a water-jumping microrobot? Experimental and theoretical investigations," *Amer. Chem. Soc. Appl. Mater. Interfaces*, vol. 4, no. 7, pp. 3706–3711, Jun. 2012.

[6] J. S. Koh et al., "Jumping on water: Surface tension–Dominated jumping of water striders and robotic insects," *Science*, vol. 349, no. 6247, pp. 517–521, Jul. 2015.

[7] F. Jiang, J. Zhao, A. K. Kota, N. Xi, M. W. Mutka, and L. Xiao, "A miniature water surface jumping robot," *IEEE Robot. Automat. Lett.*, vol. 2, no. 3, pp. 1272–1279, Jul. 2017.

[8] J. Yan, H. Yao, K. Yang, X. Zhang, and J. Zhao, "Design and simulation of a miniature jumping gliding robot on water surface," in *Proc. IEEE Int. Conf. Intell. Robot. Appl.*, 2019, pp. 715–725.

[9] T. Wang, "Research on water jumping robot inspired by water strider," M.S. thesis, Dept. Mech. Eng., HIT, Harbin, China, 2015.

[10] H. Kim, M. Sitti, and T. Seo, "Tail-assisted mobility and stability enhancement in yaw/pitch motions of a water-running robot," *IEEE/ASME Trans. Mechatron.*, vol. 22, no. 3, pp. 1207–1217, Jun. 2017.

[11] H. Kim, K. Jeong, and T. Seo, "Analysis and experiment on the steering control of a water-running robot using hydrodynamic forces," *J. Bionic Eng.*, vol. 14, no. 1, pp. 34–46, Mar. 2017.

[12] H. Kim, D. Lee, K. Jeong, and T. Seo, "Water and ground-running robotic platform by repeated motion of six spherical footpads," *IEEE/ASME Trans. Mechatron.*, vol. 21, no. 1, pp. 175–183, Feb. 2016.

[13] J. W. Glasheen and T. A. Mcmahon, "A hydrodynamic model of locomotion in the Basilisk Lizard," *Nature*, vol. 380, no. 6572, pp. 340–342, Mar. 1996.

[14] J. W. Glasheen and T. A. Mcmahon, "Size-dependence of water-running ability in basilisk lizards (Basiliscus basiliscus)," *J. Exp. Biol.*, vol. 199, no. 12, pp. 2611–2618, Dec. 1996.

[15] J. W. Glasheen and T. A. Mcmahon, "Vertical water entry of disks at low Froude numbers," *Phys. Fluids*, vol. 8, no.no. 8, pp. 2078–2083, Apr. 1996.

[16] S. Floyd, T. Keegan, J. Palmisano, and M. Sitti, "A novel water running robot inspired by basilisk lizards," in *Proc. IEEE Int. Conf. Intell. Robots Syst.*, 2006, pp. 5430–5436.

[17] S. Floyd, S. Adilak, S. Ramirez, R. Rogman, and M. Sitti, "Performance of different foot designs for a water running robot," in *Proc. IEEE Int. Conf. Robot. Automat.*, 2008, pp. 244–250.

[18] J. Zhao, T. Zhao, N. Xi, M. W. Mutka, and L. Xiao, "MSU tailbot: Controlling aerial maneuver of a miniature-tailed jumping robot," *IEEE/ASME Trans. Mechatron.*, vol. 20, no. 6, pp. 2903–2914, Dec. 2015.

[19] J. Zhao, N. Xi, B. Gao, M. W. Mutka, and L. Xiao, "Development of a controllable and continuous jumping robot," in *Proc. IEEE Int. Conf. Robot. Automat.*, 2011, pp. 4614–4619.
[20] V. H. Wagner, "Phenomena associated with impacts and sliding on liquid surfaces," *J. Appl. Math. Mechanics*, vol. 12, no. 4, pp. 193–215, 1932.
[21] S. Okada and Y. Sumi, "On the water impact and elastic response of a flat plate at small impact angles," *J. Mar. Sci. Technol.*, vol. 5, pp. 31–39, Sep. 2000.
[22] M. R. Moore, "Introducing pre-impact air-cushioning effects into the Wagner model of impact theory," *J. Eng. Math.*, vol. 129, Jun. 2021, Art. no. 6.
[23] P. Gallina, G. Bulian, and G. Mosetti, "Water bouncing robots: A first step toward large-scale water running robots," *Robotica*, vol. 34, no. 7, pp. 1659–1676, Jul. 2016.
[24] X. Zhang, J. Feng, K. Lin, and J. Hu, "Added mass of trans-media moving object," *J. Beijing Univ. Aeronaut. Astronaut.*, vol. 42, no. 4, pp. 821–828, Apr. 2016.
[25] Y. Wang and X. Shi, "Current state and progress of research on the problem of water entry impact," *Explosion Shock Waves*, vol. 28, no. 3, pp. 276–282, May 2008.
[26] K. Zhao, "Dynamics modeling and simulation of hydroplaning," M.S. thesis, Dept. Astronaut., HIT., Harbin, China, 2014.
[27] B. Chang, E. Virot, J. Myeong, H. Y. Kim, C. Clanet, and S. Jung, "Jumping dynamics of aquatic animals," *J. Roy. Soc. Interface*, vol. 16, no. 152, Mar. 2019, Art. no. 20190014.
[28] Q. Yang and W. Qiu, "Numerical simulation of water impact for 2D and 3D bodies," *Ocean Eng.*, vol. 43, pp. 82–89, Apr. 2012.
[29] M. Greenhow and S. Moyo, "Water entry and exit of horizontal circular cylinders," *Philos. Trans. Roy. Soc. London Ser. A, Math., Phys. Eng. Sci.*, vol. 355, no. 1724, pp. 551–563, Mar. 1997.
[30] Y. Lu, T. Xiao, and Z. Li, "Numerical simulation of high speed plate ditching," *Acta Aeronautica Astronautica Sin.*, vol. 38, no. S1, pp. 6–14, Dec. 2017.
[31] X. Zhang, J. Yan, K. Yang, J. Zhao, and S. Tang, "A rapid water sliding robot optimized by bionic motion trajectory," *IEEE Robot. Automat. Lett.*, vol. 7, no. 2, pp. 2463–2470, Apr. 2022.

Jihong Yan (Member, IEEE) received the B.S. and Ph.D. degrees in mechanical engineering from Harbin Institute of Technology, Harbin, China, in 1997 and 2005, respectively.

She is currently a Professor with the State Key Laboratory of Robotics and Systems, Harbin Institute of Technology. Her research interests include bionic and soft robot.

Xin Zhang (Student Member, IEEE) received the B.S. degree in mechanical engineering and automation from Sichuan University, Chengdu, China, in 2016. He is currently working toward the Ph.D. degree in mechanical engineering with the State Key Laboratory of Robotics and Systems, Harbin Institute of Technology, Harbin, China.

His research interests include bionic robots, and water jumping robot and mechanism design.

Kai Yang received the B.S. and Ph.D. degrees in mechatronics engineering from Harbin Institute of Technology, Harbin, China, in 2014 and 2021, respectively.

His research interests include bionic water sliding robots and mechanism design, and he is a senior engineer at AVIC Nanjing Engineering Institute of Aircraft Systems.

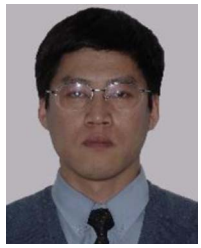

Jie Zhao (Member, IEEE) received the B.S. and Ph.D. degrees in mechatronics engineering from Harbin Institute of Technology, Harbin, China, in 1990 and 1996, respectively.

He is the Head of Robotics Institute and School of Mechatronics Engineering, Harbin Institute of Technology. He is also the Leader of the Subject Matter Expert Group of Intelligent Robot in National 863 Program.